An Explicit Nonlinear Model Predictive ABS Controller for Electro-Hydraulic Braking Systems

Davide Tavernini , Fabio Vacca , Mathias Metzler , *Graduate Student Member, IEEE,*
Dzmitry Savitski , *Member, IEEE,* Valentin Ivanov , *Senior Member, IEEE,* Patrick Gruber ,
Ahu Ece Hartavi, Miguel Dhaens, and Aldo Sorniotti , *Member, IEEE*

Abstract—**This paper addresses the development and Hardware-in-the-Loop (HiL) testing of an explicit nonlinear model predictive controller (eNMPC) for an antilock braking system (ABS) for passenger cars, actuated using an electro-hydraulic braking unit. The control structure includes a compensation strategy to guard against the performance degradation due to actuation dead times, identified by experimental tests. The eNMPC is run on an automotive rapid control prototyping unit, which shows its real-time capability with comfortable margin. A validated high-fidelity vehicle simulation model is used for the assessment of the ABS on a HiL rig equipped with the braking system hardware. The eNMPC is tested in seven emergency braking scenarios, and its performance is benchmarked against a proportional-integral-derivative (PID) controller. The eNMPC results show: 1) the control system robustness with respect to the variations in tire-road friction condition and initial vehicle speed; and 2) consistent and significant improvement of the stopping distance and wheel slip reference tracking, with respect to the vehicle with the PID ABS.**

Index Terms—**Antilock braking system (ABS), wheel slip control, explicit nonlinear model predictive control (eNMPC), Hardware-in-the-Loop (HiL), electro-hydraulic braking (EHB) system.**

I. INTRODUCTION

ELECTRO-HYDRAULIC braking (EHB) systems are becoming viable solutions for conventional, hybrid electric, and fully electric vehicles, as demonstrated by the first successful implementations on series passenger cars [1]–[3]. In EHB systems, the brake pedal and wheel calipers are decoupled to allow pedal force feedback and, thus, pedal feeling that is independent of the operating conditions of the braking system. In addition to the driver's comfort benefit, EHB units permit continuous control of each caliper pressure. This is ideal for brake blending, i.e., the seamless and variable braking torque distribution between friction brakes and electric drivetrains.

Also, compared to standard braking systems with vacuum booster, EHB systems allow relatively smaller packaging and faster response times [4]. The quicker response is beneficial to the performance of active safety functions such as electronic stability control [5].

Antilock braking systems (ABS) for passenger cars were developed to increase road safety by keeping the vehicle steerable and stable during intense braking events, especially on slippery road surfaces [6], [7]. The first implementations used rule-based algorithms considering the estimated slip ratio and wheel deceleration. These controllers were suitable for hydraulic units capable of generating sequences of pressure increase, decrease, and hold phases, but without the capability of continuous feedback control. Such algorithms were rather robust with respect to the possible operating conditions of the vehicle, but they provided suboptimal performance in terms of wheel slip tracking. Since then, improvements have been gradually implemented at the cost of increased tuning complexity [8]. Nevertheless, today's industrial ABS control strategies are still based on a complex set of rules. The EHB technology, similarly to the electro-mechanical brake technology, permits more refined wheel slip control with continuous braking torque modulation [9]. Algorithms based on proportional-integral-derivative (PID) formulations [10], [11], second-order sliding mode [12], as well as maximum transmissible torque estimation [13] have been proposed for ABS or traction control. Furthermore, Fujimoto *et al.* [14] discusses a selection of wheel slip controllers for electric vehicles, not requiring vehicle speed detection, while Wang *et al.* [15] presents slip controllers for split-μ conditions.

The recent literature shows increasing interest in model-based state feedback controllers, especially in model predictive control (MPC). In [16], an ABS based on a gain-scheduled linear quadratic regulator was tested on a vehicle with electro-mechanical brake calipers. Linear MPCs are discussed in [17]–[19], in the context of ABS including torque blending between friction brakes and in-wheel motors. In [20], the MPC strategy is compared with a PI controller and is assessed on an electric vehicle prototype. A linear MPC is also presented in [21], with

the results from a Hardware-in-the-Loop (HiL) rig including a brake-by-wire system. This paper shows the deterioration of the longitudinal slip tracking performance during transitions from high to low tire-road friction levels.

Borrelli *et al.* [22] discusses a traction controller for an internal-combustion-engine-driven vehicle and compares four linear MPC strategies with a hybrid explicit MPC. The performance of the hybrid strategy is comparable with that of a well-tuned PID controller. Basrah *et al.* [23] presents a real-time capable implicit nonlinear model predictive controller (NMPC) for an ABS with torque blending and compares the NMPC simulation results with those from a linear MPC. In addition to the better performance of the nonlinear solution, Basrah *et al.* [23] reports that the computational time for the NMPC is of 3–4 ms on a desktop personal computer, whereas the linear MPC requires ∼1 ms. In [24], an implicit NMPC slip-control strategy is assessed in simulation, and it was implemented on a quad-core 2.8-GHz dSPACE unit, yielding a computational time of 4–5 ms. Tavernini *et al.* [25] shows that the implementation time step is more influential than the selected control technology (NMPC or PID) on the performance of a traction controller for an electric vehicle with in-wheel motors. Hence, controllers with high tracking performance and low computing times are required for effective wheel slip control.

In this context, this paper presents an explicit NMPC algorithm—so-called explicit nonlinear model predictive controller (eNMPC)—for ABS, and its implementation on an EHB system. The eNMPC is selected for the following reasons:

1) According to many practitioners, MPC represents the future of automotive control, since this technology: a) requires a lower number of calibration parameters than that required by more conventional controllers, and thus reduces development times, as stated in [22], [26], and [27]; b) permits formal consideration of system constraints; and c) allows preview control, which is of the essence in the future context of connected and autonomous vehicles. In such implementations, the tire-road friction estimation could be enhanced by the information from the vehicles located in front of the ego vehicle, and in general the characteristics of the road ahead are likely to be better known than that in the existing controllers. The eNMPC ABS of this research prepares the ground for these developments, as the tire-road friction coefficient can be included as an input parameter varying in real-time.

2) NMPC for ABS control offers benefits with respect to alternative control technologies, such as H_∞ control and sliding mode control [10]. The main issue of H_∞ control is that the range of variation of the longitudinal tire slip stiffness is too wide to be captured by a single controller based on a linear model with fixed longitudinal slip stiffness. Moreover, wheel slip control interventions are becoming more frequent in modern stability controllers actuating the friction brakes, which tend to operate to improve the cornering response also in sublimit conditions as seamlessly as possible. Hence, it is desirable to have a controller capable of a rather smooth wheel slip
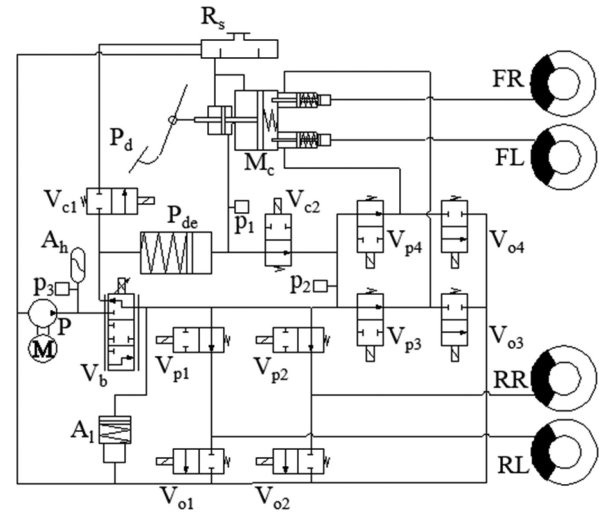
Fig. 1. Simplified hydraulic schematic of the case study SCB unit.

control action, without the typical chattering issues of sliding mode controllers.

3) Because of its explicit nature, the specific ABS eNMPC of this paper requires only a fraction of the computing time (i.e., < 0.1 ms on a 900-MHz dSPACE automotive platform) of the implicit solutions in [23] and [24], and therefore can run at much smaller time steps than an equivalent implicit NMPC.

4) In eNMPC, the explicit solution is known in advance, which allows carrying out a systematic *a priori* analysis of the control system performance, with benefits in terms of functional safety of the automotive system, with respect to implicit NMPC.

The following are the points of novelty:

1) The design and experimental implementation of a proof-of-concept eNMPC ABS based on continuous wheel slip control. The algorithm takes the experimentally measured dead time of the hydraulic components into account using a compensation strategy.

2) The comparison of the eNMPC ABS with a benchmark PID controller, including robustness assessment with respect to tire-road friction conditions and initial vehicle speed.

II. PLANT

A. EHB System

This paper uses the slip control boost (SCB) unit by ZF-TRW [28]. Fig. 1 shows the schematic of the hydraulic circuit of the EHB system including the four brake calipers. The notations FL, FR, RL, and RR indicate the front left, front right, rear left, and rear right corners, respectively. The driver demand is measured in terms of brake pedal displacement (P_d) and pressure at the normally open valve V_{c2}, which is activated upon brake application. A brake pedal force emulator (P_{de}) provides force feedback to the driver. The measured signals are transmitted to the brake function control unit that calculates the caliper

TABLE I
MAIN BRAKE CORNER PARAMETERS

Symbol	Description	Value	Unit
$R_{m,F}$	Front equivalent brake disc radius	0.120	m
$R_{m,R}$	Rear equivalent brake disc radius	0.133	m
$D_{wc,F}$	Front brake piston diameter	0.057	m
$D_{wc,R}$	Rear brake piston diameter	0.040	m
μ_{brk}	Brake-disc-to-pad friction coefficient	0.400	(-)
K_F	Front torque-to-pressure coefficient	0.041	bar/Nm
K_R	Rear torque-to-pressure coefficient	0.075	bar/Nm

pressure demands. These are sent to the electro-hydraulic control unit (EHCU), which tracks them through a combination of feedback and open-loop control of the EHB valves and motor. A feedback pressure controller modulates the proportional boost valve, V_b, either to increase the brake pressure in the rail leading to the four inlet valves, V_{p1}–V_{p4}, or to decrease it by sending the fluid back to the reservoir, R_s. The high pressure accumulator, A_h, is charged up to 180 bar by the electric pump, P, to ensure a fast system response during the pressure increase phases. In normal braking conditions, V_{p1}–V_{p4} remain open to permit the fluid to reach the calipers, and the four outlet valves, V_{o1}–V_{o4}, are closed. During the operation of the ABS and stability control system, individual caliper pressure modulation is achieved by the open-loop digital control of the inlet and outlet valves. The low pressure accumulator, A_1, provides the brake fluid volume displacement to prevent significant pressure oscillations.

The brake torque is proportional to caliper pressure, which generates the clamping force between pads and disks. The torque-to-pressure coefficient, K_i, for each corner of the ith axle (i.e., F for front and R for rear) is given by

$$K_i = \frac{1}{2\mu_{\text{brk}}A_{wc,i}R_{m,i}} \quad i \in \{F, R\} \tag{1}$$

where μ_{brk} is the friction coefficient (assumed constant) between the pads and disk, $A_{wc,i}$ is the area of the brake caliper piston of diameter $D_{wc,i}$, i.e., $A_{wc,i} = \frac{\pi}{4}D_{wc,i}^2$, and $R_{m,i}$ is the equivalent brake disk radius. The main braking corner parameters of the case study vehicle are reported in Table I.

B. HiL Setup

The HiL testing facility (see Fig. 2) used for the experiments of this paper consists of the following hardware components:
1) The EHB system described in Section II-A, with its EHCU;
2) The brake calipers and disks of the four corners of the case study vehicle;
3) Pressure sensors located close to the calipers to monitor the actual brake pressures;
4) The real-time testing platform dSPACE DS1006 (quad-core, 2.8 GHz), running a high-fidelity vehicle simulation model.

The vehicle simulator is an experimentally validated (see [29] and [30]) IPG CarMaker HiL model. The tire model is the Pace-jka Magic Formula (MF) (ver. 5.2) [31], with varying longitudinal tire relaxation length as a function of both vertical load and
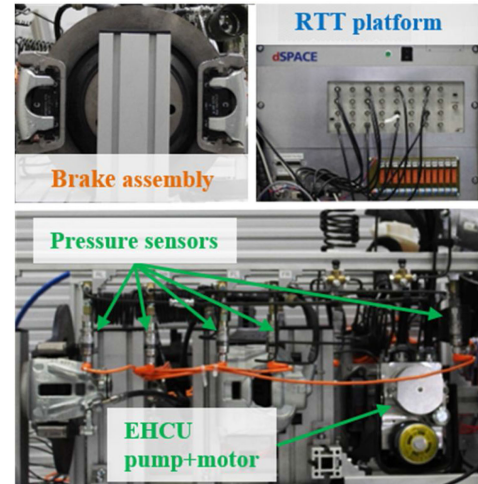
Fig. 2.   HiL test rig of the Technische Universität Ilmenau.
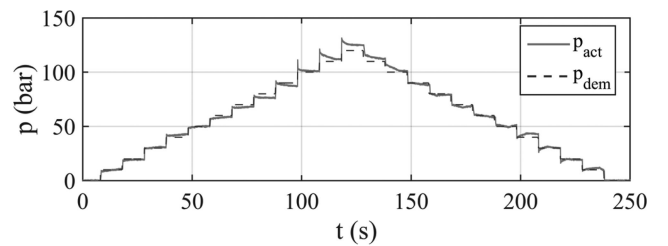
Fig. 3.   Time history of a 10-bar staircase p_{dem} test for a front caliper.

longitudinal slip, as described in [32]. The experimental caliper pressure measurements are sent to the real-time vehicle simulator, which calculates the braking torque, and thus the overall vehicle dynamics, from the torque-to-pressure coefficients of the respective calipers.

C. EHB System Characterization

Experimental tests with different caliper pressure demand (p_{dem}) profiles were carried out to determine the brake pressure response characteristics. The measurements focused on the computation of the following:
1) The dead time, Δ_i, i.e., the time required to achieve 1 bar variation of the actual caliper pressure, p_{act}, from when a p_{dem} step is requested;
2) The rise time, r_i, i.e., the time required for p_{act} to increase from 10% to 90% of its steady-state reference value during a p_{dem} step request.

Δ_i and r_i were assessed from 10 repeated staircase tests, consisting of 12 steps of p_{dem} with a 10-bar amplitude each (see Fig. 3). The staircase tests simultaneously involved all the four calipers, and they can be considered representative of the ABS regulation condition as a nonzero pressure is present in all the calipers. Fig. 4(a) and (c) report the average values and error bars of Δ_i for the front and rear calipers, as functions of the final p_{dem} values at each step. The magnitude of the error bar represents the standard deviation of the measured values for the

Fig. 4. Average values and error bars of: the (a) front and (c) rear caliper pressure dead times (Δ_i), and the (b) front and (d) rear caliper pressure rise times (r_i), as functions of the final value of p_{dem} for 10 repetitions of the 10-bar staircase test.

Fig. 5. Sine sweep test on the front left caliper: average pressure of 100 bar, reference amplitude of 20 bar, and maximum frequency of 7 Hz.

10 test repetitions. The average r_i values and respective error bars are shown in Fig. 4(b) and (d). In addition, Fig. 5 reports the time–pressure history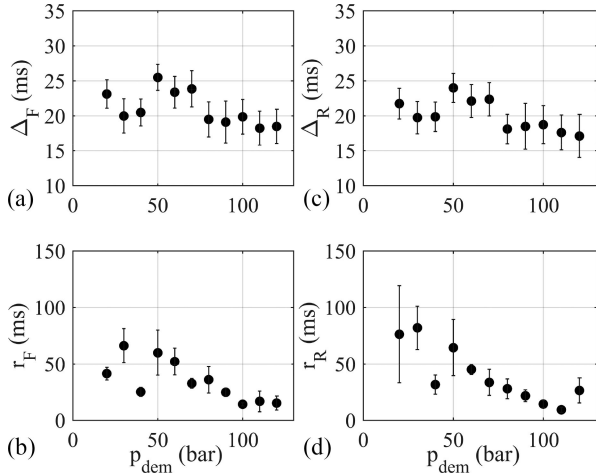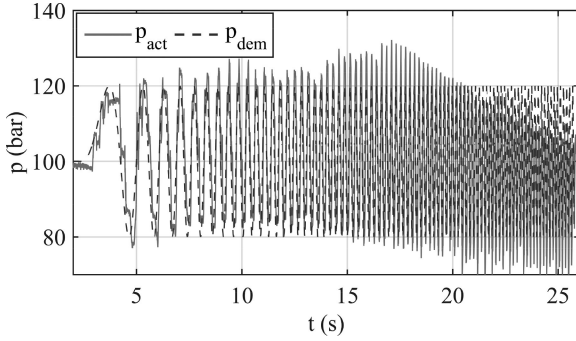 for a sine sweep test on the front left caliper, with an amplitude of 20 bar and a linearly increasing frequency (up to 7 Hz) of p_{dem}, around a value of 100 bar.

The results confirm the significant nonlinearity of the system response. In particular, Δ_i and r_i tend to decrease with increasing p_{dem}. The average dead time, of approximately 20 ms, is long compared to the typical implementation time step of an ABS algorithm (see Section I), which makes continuous wheel slip control rather difficult. Nevertheless, the EHB has very good dynamic characteristics and accurate pressure tracking capabilities relative to a conventional automotive braking system with vacuum booster.

III. EXPLICIT NONLINEAR MPC

A. General Optimal Control Problem Formulation

The eNMPC requires the formulation of an optimization problem, where constraints on the control inputs and system states can be imposed. For a finite horizon in the time interval $[t_k, t_f]$, a generic nonlinear optimal control problem is defined to minimize the following cost function:

$$V\left(x\left[t_k, t_f\right], u\left[t_k, t_f\right], p\left(t_k\right), \nu\left[t_k, t_f\right]\right)$$
$$\triangleq \int_{t_k}^{t_f} L\left(x\left(t\right), u\left(t\right), p\left(t_k\right), \nu\left(t\right), t\right) dt + M\left(x\left(t_f\right), p\left(t_k\right), t_f\right) \tag{2}$$

where x, u, p, and ν are the state, input, parameter (including system and controller parameters, considered constant for the duration of the prediction horizon), and slack variable vectors, which are internally normalized by a set of characteristic values; t is time; L is the stage cost; M is the terminal cost. The problem is subject to the following inequality constraints:

$$x_{\min} \leq x\left(t\right) \leq x_{\max} \tag{3}$$
$$u_{\min} \leq u\left(t\right) \leq u_{\max} \tag{4}$$
$$g\left(x\left(t\right), u\left(t\right), p\left(t_k\right), \nu\left(t\right), t\right) \leq 0. \tag{5}$$

The equality constraints are the following ordinary differential equations describing the system dynamics:

$$\frac{d}{dt} x\left(t\right) = f\left(x\left(t\right), u\left(t\right), p_s\left(t_k\right), t\right) \tag{6}$$

where p_s is the vector of the system parameters, and $x(t_k)$ is imposed as initial condition vector.

The infinite-dimensional optimal control problem in (2)–(6) is discretized and parametrized, thus becoming a nonlinear programming (NLP) problem, which is solved using numerical methods. In this operation, known as direct method [33], the equality constraints (6) are represented by finite approximations. The infinite-dimensional unknown solution, $u[t_k, t_f]$, and the slack variables, $\nu[t_k, t_f]$, are replaced by a finite number of decision variables. The prediction horizon, $t_p = t_f - t_k$, is defined as $t_p = N_p t_s$, where N_p is the number of prediction steps and t_s is the discretization interval of the internal model. The input, $u[t_k, t_f]$, is assumed piecewise constant along the horizon. u is calculated using a function γ and is expressed using the control parameterization vector, U, so that $u(t) = \gamma(t, U)$. Similarly, the slack variable vector is parameterized using the vector N, i.e., $\nu(t) = \xi(t, N)$.

The technique known as direct single shooting [34]–[36] deals with the equality constraints. They are eliminated by substituting their discretized numerical solution (only function of the initial conditions at t_k) into the cost function and constraint functions. The optimal control problem is now in its multiparametric (mp) NLP generic form as follows:

$$V^*\left(x\left(t_k\right), p\left(t_k\right)\right) = \min_{U, N} V\left(x\left(t_k\right), U, p\left(t_k\right), N\right) \tag{7}$$

subject to

$$G\left(x\left(t_k\right), U, p\left(t_k\right), N\right) \leq 0. \tag{8}$$

Two additional vectors are defined as follows:
1) The problem parameter vector, $x_p(t_k) \in \mathbb{R}^{n_p}$, with $n_p = n + d$, i.e., n_p is the sum of the number of states, n, and

the number of parameters, d, of the system and controller:

$$x_p(t_k) = [x(t_k), p(t_k)] \quad (9)$$

2) The decision variables vector, $z \in \mathbb{R}^s$:

$$z = [U, N]. \quad (10)$$

From (9) and (10) it is possible to reformulate (7) and (8) as

$$V^*(x_p(t_k)) = \min_z V(z, x_p(t_k)) \quad (11)$$

subject to

$$G(z, x_p(t_k)) \leq 0. \quad (12)$$

The minimization is performed with respect to z and is parameterized with $x_p(t_k)$.

B. Offline Solution and Online Evaluation

The mp-NLP problem is not solved directly, but using a mp quadratic programming (mp-QP) approximation (see [34] and [35]) of the mp-NLP, as suggested in [33] and implemented in [36]. The mp-NLP in (11) and (12) is linearized around a point $(z_0, x_{p,0})$ by means of Taylor series expansion. The cost function is, thus, approximated using a quadratic function, and the constraints assume a linear form.

The mp-QP formulation is used to generate local approximations of the original mp-NLP problem within the exploration space, which consists of a number of hyper-rectangles, on which single mp-QP problems are solved. Each hyper-rectangle is further partitioned into polyhedra, i.e., the critical regions for the mp-QP problem. The resulting solution is a piecewise affine function, which is continuous across the boundaries of different polyhedra but discontinuous across the hyper-rectangles.

The Multi-Parametric Toolbox 3.0 [37] is employed for the computation of the mp-QP problems. The solution is evaluated at points of interest within the hyper-rectangles and compared with the NLP solution at the same points, which is computed using IPOPT, a software package for nonlinear optimization [38]. The maximum error on the cost function, decision variables, and constraints' violation between the evaluated mp-QP and computed NLP solutions are observed for all the considered points. This allows deciding whether to stop the process and accept the mp-QP approximating solution or to subpartition the hyper-rectangles into smaller ones using heuristic splitting rules similar to those in [33]. When the algorithm terminates, the explicit solution is available for any point inside each hyper-rectangle. The explicit solution of this paper consists of 123 hyper-rectangles, each one including a number of polyhedra ranging from 1 to 68. The associated real-time program requires <16 MB of memory to run. This is in line with the new generation of microcontrollers for automotive applications, which will be available in the market soon.

The next step is the online implementation of the previous offline solution. This is performed using point location and piecewise control function evaluation through two layers based on
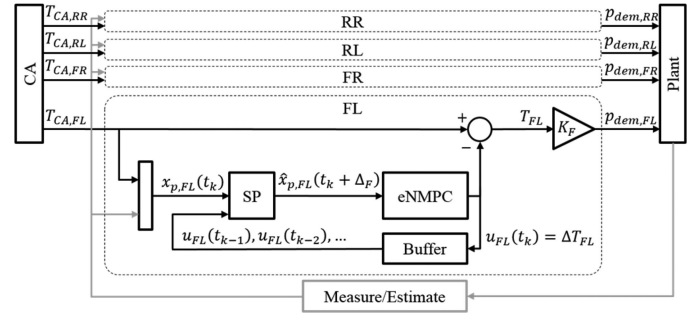

Fig. 6. Simplified architecture of the ABS control strategy.

the binary-search-tree method [39]. The top layer determines the index of the hyper-rectangle that contains the point. The bottom layer identifies the correct critical region and evaluates the associated control function.

IV. CONTROLLER DESIGN

A. ABS Control Structure

The block diagram of the control system architecture is shown in Fig. 6. The brake torque demand for each corner is calculated by the control allocation (CA) algorithm. Given the seamless pressure modulation capability of the EHB, independent of the applied brake pedal force, the front-to-rear brake torque distribution can be continuously varied by using the CA algorithm. For example, a brake distribution curve close to the ideal parabolic one [40] could be achieved when the electronic brake distribution or ABS are not active.

Within the ABS controller, a state predictor (SP) and a buffer compensate the dead times Δ_i in the EHB response, as identified in Section II-C. The updated (i.e., predicted) problem parameters vector, $\hat{x}_{p,ij}$, is then sent to the eNMPC block that computes the regulating torque, ΔT_{ij}, which is subtracted from the torque, $T_{\mathrm{CA},ij}$, output by the CA algorithm. Next, the corrected wheel torque is converted into an EHB pressure demand, $p_{\mathrm{dem},ij}$, with the help of (1). In the previous notations, the subscript j indicates the location of the corner within the axle, i.e., L for left and R for right. For clarity, in the remainder of this paper, the formulations are presented for the front left (FL) corner.

B. Internal Prediction Model

The internal prediction model has been selected to be as simple as possible, while retaining important characteristics such as the nonlinear tire model formulation.

In the internal quarter car model of the eNMPC, the front left tire slip ratio, $\lambda_{x,\mathrm{FL}}$, is defined as

$$\lambda_{x,\mathrm{FL}}(t) = \frac{V_v(t) - \omega_{\mathrm{FL}}(t) R_w}{V_v(t)} \quad (13)$$

where ω_{FL} is the angular wheel velocity, R_w the rolling radius, and V_v the longitudinal vehicle speed. The time derivative of

TABLE II
eNMPC INTERNAL MODEL PARAMETERS

Symbol	Description	Value	Unit
m_i	Apparent front (rear) corner mass	750 (250)	kg
R_w	Wheel rolling radius	0.363	m
J_w	Wheel mass moment of inertia	2.21	kgm²
B	MF coefficient: stiffness factor	40	-
C	MF coefficient: shape factor	1.4	-
D	MF coefficient: peak value	0.45	-
$F_{z,i}$	Front (rear) tire vertical load	7356 (2453)	N

$\lambda_{x,\mathrm{FL}}$ is

$$\frac{d}{dt}\lambda_{x,\mathrm{FL}}(t) = \frac{\frac{d}{dt}V_v(t) - R_w\frac{d}{dt}\omega_{\mathrm{FL}}(t)}{V_v(t)}$$
$$- \frac{(V_v(t) - \omega_{\mathrm{FL}}(t)R_w)\left(\frac{d}{dt}V_v(t)\right)}{V_v^2(t)} \quad (14)$$

where the wheel rotational dynamics can be expressed as

$$\frac{d}{dt}\omega_{FL}(t) = \frac{1}{J_w}\left(F_{x,\mathrm{FL}}R_w - T_{\mathrm{CA,FL}} + \Delta T_{\mathrm{FL}}(t)\right) \quad (15)$$

J_w is the wheel mass moment of inertia. $T_{\mathrm{CA,FL}}$ is considered constant over the prediction horizon, and thus is an element of the parameter vector, p_{FL}. The longitudinal force balance of the quarter car model associated with the considered wheel is

$$\frac{d}{dt}V_v(t) = -\frac{1}{m_F}F_{x,\mathrm{FL}} \quad (16)$$

where $F_{x,\mathrm{FL}}$ is the longitudinal tire force. A simplified version of the Pacejka MF [31] is employed for the tire force characteristics as follows:

$$F_{x,\,\mathrm{FL}} = \mu_{x,\mathrm{FL}}F_{z,F} \quad (17)$$
$$\mu_{x,\mathrm{FL}} = D\sin\left(C\arctan\left(B\,\lambda_{x,\mathrm{FL}}(t)\right)\right) \quad (18)$$

where $F_{z,F}$ is the vertical tire load, considered constant. $\mu_{x,\mathrm{FL}}$ is the longitudinal tire-road friction coefficient, and B, C, and D are the MF parameters (see Table II).

By substituting (15)–(18) into (14), the following wheel slip dynamics equation, i.e., the first differential equation of the eNMPC internal model, is obtained

$$\frac{d}{dt}\lambda_{x,\mathrm{FL}}(t)$$
$$= -\frac{\left(\frac{1-\lambda_{x,\mathrm{FL}}(t)}{m_F} + \frac{R_w^2}{J_w}\right)D\sin\left(C\arctan\left(B\lambda_{x,\mathrm{FL}}(t)\right)\right)F_{z,F}}{V_v}$$
$$+ \frac{(T_{\mathrm{CA,FL}} - \Delta T_{\mathrm{FL}}(t))R_w}{J_w V_v}. \quad (19)$$

As vehicle speed has slower dynamics than $\lambda_{x,\mathrm{FL}}$, V_v is considered constant along the prediction horizon.

An integral action is incorporated in the formulation to tackle steady-state errors and model uncertainties. Hence, the internal model includes $e_{\mathrm{int,FL}}$, which is the integral of the error between the actual wheel slip, $\lambda_{x,\mathrm{FL}}$, and the reference slip, λ_x^{ref}. The $e_{\mathrm{int,FL}}$ dynamics provide the second and last differential

equation of the internal prediction model, as follows:

$$\frac{d}{dt}e_{\mathrm{int,FL}}(t) = \lambda_{x,\mathrm{FL}}(t) - \lambda_x^{\mathrm{ref}}. \quad (20)$$

The EHB actuation dynamics are not included in the internal model to verify the robustness of the controller against the variability of the actuator response. The state vector, input vector, and parameter vector are, respectively, $x_{\mathrm{FL}} = [\lambda_{x,\mathrm{FL}}, e_{\mathrm{int,FL}}]$, $u_{\mathrm{FL}} = [\Delta T_{\mathrm{FL}}]$, and $p_{\mathrm{FL}} = [V_v, T_{\mathrm{CA,FL}}, \lambda_x^{\mathrm{ref}}]$. A prediction horizon $t_p = 9\,\mathrm{ms}$ (i.e., $N_p = 3$ steps and $t_s = 3\,\mathrm{ms}$) is selected for the current implementation. The problem includes five parameters [five-dimensional (5-D) problem], i.e., $x_{p,\mathrm{FL}}(t_k) = [\lambda_{x,\mathrm{FL}}(t_k), e_{\mathrm{int,FL}}(t_k), V_v(t_k), T_{\mathrm{CA,FL}}(t_k), \lambda_x^{\mathrm{ref}}(t_k)]$, and four decision variables, i.e., $z_{\mathrm{FL}} = [\Delta T_{\mathrm{FL}}(t_k), \Delta T_{\mathrm{FL}}(t_{k+1}), \Delta T_{\mathrm{FL}}(t_{k+2}), v_{1,\mathrm{FL}}(t_k)]$. $v_{1,\mathrm{FL}}$ is the slip ratio slack variable. The control horizon is equal to t_p. Longer horizons were also considered in this paper and tested in simulation. The final selection was based on the tracking performance of the controller (i.e., the RMS value of the slip ratio error) and the vehicle deceleration profile, which resulted better for $t_p = 9\,\mathrm{ms}$.

Table II reports the values of the internal model parameters. The apparent front and rear corner masses have been defined to obtain the same deceleration for the four quarter car models for specific operating conditions; i.e., the 75/25 front-to-rear mass ratio corresponds to the ideal braking distribution ratio for a longitudinal vehicle deceleration of 6 m/s². Constant m_i values are used for all braking tests.

C. Optimal ABS Control Problem Formulation

The continuous form of the cost function to be minimized during the offline optimization process is

$$V_{\mathrm{FL}} = \int_{t_k}^{t_f}\left[\frac{q_{x1}}{w_{x1}^2}\left(\lambda_{x,\mathrm{FL}}(t) - \lambda_x^{\mathrm{ref}}(t_k)\right)^2 + \frac{q_{x2}}{w_{x2}^2}e_{\mathrm{int,FL}}(t)^2\right.$$
$$\left. + \frac{r_u}{w_u^2}\Delta T_{\mathrm{FL}}(t)^2 + \frac{r_\nu}{w_\nu^2}\nu_{1,\mathrm{FL}}(t_k)^2\right]dt + \frac{p_{x1}}{w_{x1}^2}$$
$$\times \left(\lambda_{x,\mathrm{FL}}(t_f) - \lambda_x^{\mathrm{ref}}(t_k)\right)^2 + \frac{p_{x2}}{w_{x2}^2}e_{\mathrm{int,FL}}(t_f)^2 \quad (21)$$

where $q_{x1} = 5$, $q_{x2} = 60$, $r_u = 10$, $r_\nu = 10$, $p_{x1} = 5$, and $p_{x2} = 60$ are the weights for the different terms, and $w_{x1} = 0.1$, $w_{x2} = 0.1$, $w_u = 3000$, and $w_v = 0.5$ are the scaling factors.

As a consequence, a tracking problem is set for the first state, $\lambda_{x,\mathrm{FL}}$, and a regulating problem is set for the second state, $e_{\mathrm{int,FL}}$.

The minimization of (21) is subject to the following state and input bound constraints:

$$\lambda_{x,\min} - \nu_{1,\mathrm{FL}}(t_k) \le \lambda_{x,\mathrm{FL}}(t) \le \lambda_{x,\max} + \nu_{1,\mathrm{FL}}(t_k) \quad (22)$$
$$\Delta T_{\min} \le \Delta T_{\mathrm{FL}}(t) \le \Delta T_{\max} \quad (23)$$

where $\Delta T_{\max} = T_{\mathrm{CA,FL}}$ and $\Delta T_{\min} = 0$, while $\lambda_{x,\min}$ and $\lambda_{x,\max}$ are used as tuning parameters.

D. ABS Explicit Solution

Fig. 7 is a graphic representation of the 5-D explicit solution computed offline. Three of the five parameters are fixed for
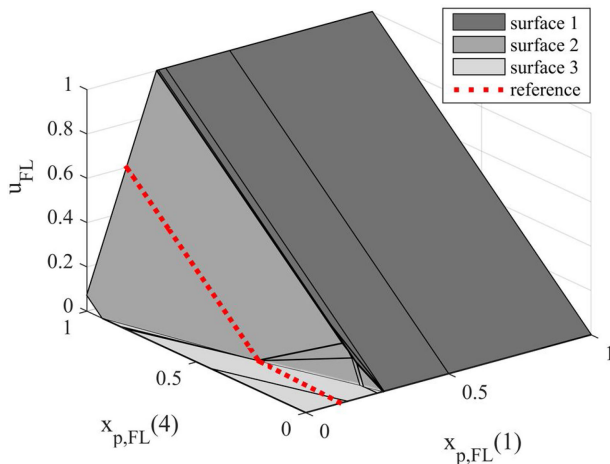
Fig. 7. Representation of the explicit solution of the control problem for fixed values of the integral of the slip ratio error, vehicle velocity, and reference slip ratio (dashed line). $x_{p,\mathrm{FL}}(1)$ and $x_{p,\mathrm{FL}}(4)$ are the normalized input parameters; u_{FL} is the normalized eNMPC control action.

ease of visualization. In particular, the normalized value of the integral of the slip error, $x_{p,\mathrm{FL}}(2)$, is set to 0; the normalized value of vehicle speed, $x_{p,\mathrm{FL}}(3)$, is set to a value corresponding to 90 km/h; the normalized value of the reference slip ratio, $x_{p,\mathrm{FL}}(5)$, is set to a value corresponding to 0.07. Each normalization is performed using the characteristic values for the specific application.

The figure reports the normalized control variable, u_{FL}, for a combination of the normalized values of slip ratio, $x_{p,\mathrm{FL}}(1)$, and torque demand from the CA algorithm, $x_{p,\mathrm{FL}}(4)$. Fig. 7 also indicates the polyhedral regions belonging to different hyper-rectangles, resulting from the generation of the explicit solution.

The control action consists of three main surfaces. Surfaces 1 and 3 represent the upper and lower input constraints described by (23). Surface 2 represents the nonsaturated control law, which is close to linearity for most of the input parameter values. The red-dashed line, indicated as the reference in the legend, represents the imposed constant slip reference for this explanatory example.

For small values of $x_{p,\mathrm{FL}}(4)$, the torque regulation u_{FL} is not necessary, even for slip ratio values slightly higher than the reference. In fact, in such cases, the internal model predicts that the wheel will return to low slip values without intervention. In general, despite the possibility of discontinuities of the explicit solution across the hyper-rectangles, the specific ABS implementation shows significant smoothness of the resulting control action.

In the online implementation, the measured or estimated input parameters would normally be sent directly to the eNMPC. However, given the significance of the identified EHB system's dead times, a compensation algorithm is implemented using a concept similar to the one in [22] and [41]. An SP based on the model formulation presented in Section IV-B and a buffer for the past control history predict the parameter trajectory for a horizon length corresponding to the dead time. The inputs to

the controller are, thus, projected into the future, and the control action is evaluated for the final values of this prediction.

With respect to stability, common schemes in the literature for implicit MPC include stabilizing terminal constraints or terminal costs, which need to satisfy Lyapunov-function-type conditions [42], [43]. Alternatively, [44] and [45] present techniques for evaluating the stability and performance in NMPC schemes without stability-preserving constraints. However, all these approaches are intended for implicit MPC. To the best of the authors' knowledge, no comparable practical theory is available in the literature to address eNMPC stability. Nevertheless, for this paper, the control system stability is verified via Monte Carlo simulations, as described in Section V.

To assess the computational load due to the evaluation of the eNMPC solution for a comprehensive grid of possible inputs, the controller implementation was initially tested on a dSPACE MicroAutobox II (900 MHz, 16 MB) rapid control prototyping unit, before its installation on the HiL rig. The resulting computational time was always less than 95 μs, which proves that the eNMPC can run in real-time with virtually any desired time step for the ABS application. For the specific implementation of this paper, the time step adopted for the update of the braking torque corrections was 3 ms.

V. ROBUST STABILITY ANALYSIS VIA MONTE CARLO SIMULATIONS

To ensure that the controller is stable and provides good performance for widely varying conditions of the real system, the eNMPC strategy was tested on a large number of challenging scenarios by conducting a Monte Carlo analysis. To do so, the IPG CarMaker model used for the vehicle plant in the HiL setup (see Section II-B) was employed in a software-in-the-loop fashion. The actuators' dynamics and pure time delays were included in the model and parameterized on the basis of the measurements presented in Fig. 4. Similarly to Section VI, starting from a constant speed, straight-line braking maneuvers with ABS intervention were simulated.

For the generation of the Monte Carlo test scenarios, the following six critical parameters were varied:

1) The initial speed of the braking maneuver, $V_{v,\mathrm{init}}$;
2) The friction coefficient of the road, μ;
3) The vehicle mass (by adding mass, m_{add}, to the unladen vehicle mass);
4) The dead times, Δ_i, of the EHB system at the four vehicle corners;
5) The reference slip ratio for ABS control, λ_x^{ref};
6) The scaling factor, W_σ, of the longitudinal tire force relaxation length.

The Monte Carlo analysis included 1000 test scenarios, defined by the combination of randomly chosen values of the parameters, each of them possessing a specific probability distribution. Fig. 8(a)–(d) shows the distribution of the considered values for the six parameters. This was created by assuming that: 1) the variation of the initial speed follows a uniform distribution between an upper bound and a lower bound; and 2) the tire-road friction coefficient, additional mass, pure time delay,
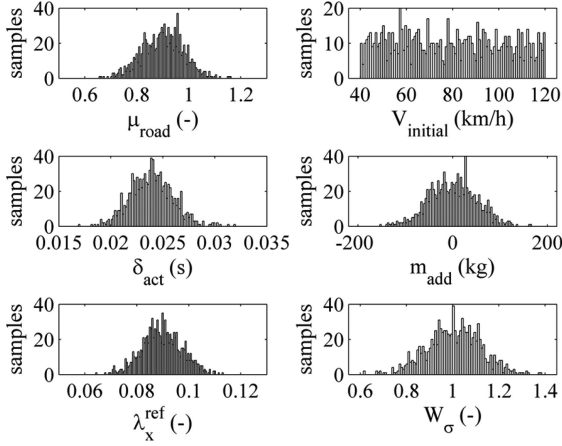
Fig. 8. Parameters values distribution for the Monte Carlo analysis.

TABLE III
MONTE CARLO ANALYSIS RESULTS

Test ID	Number of simulated scenarios	$\tau_{ths,\%}$	Instability rate**
A*	1000	10%	0%
B	1000	5%	1.3%

*Analysis requirement
**Percentage of total scenarios where instability was detected

reference slip ratio, and relaxation length scaling factor have a normal distribution, which has been tuned to fulfil realistic bounds.

Regarding the assessment of the controller's performance, instability was defined on the basis of the European regulation for vehicles equipped with ABS [46], which states that only brief periods of wheel locking are allowed. Hence, the controller was assumed unstable when a locked wheel was detected for a continuous period of time greater than a specified percentage threshold, $\tau_{ths,\%} = 10\%$, of the total duration of the ABS braking maneuver.

As indicated by the results of the simulated scenarios in Table III, instability conditions (as low as 1.3% of the tests) are only observed for $\tau_{ths,\%} = 5\%$, while the greater threshold yields 0% instability rate. This behavior can be deemed satisfactory, as all the instability conditions were detected for $\tau_{ths,\%} < 10\%$, and mostly in scenarios with low initial speed, which are commonly considered less safety critical. It was also verified that the controller never brings any corner to operate in free-wheeling conditions because of excess of ABS regulation. In conclusion, the eNMPC controller can be considered very resilient in terms of robust stability.

VI. EXPERIMENTAL SETUP AND RESULTS

The performance of the eNMPC ABS is assessed by simulating a straight-line braking maneuver according to the ISO standard 21994:2007 [47] on the HiL rig (see Section II). The maneuver is started from a vehicle speed, $V_{v,\text{init}}$, of 100 km/h, with the transmission set to neutral and the clutch disengaged.
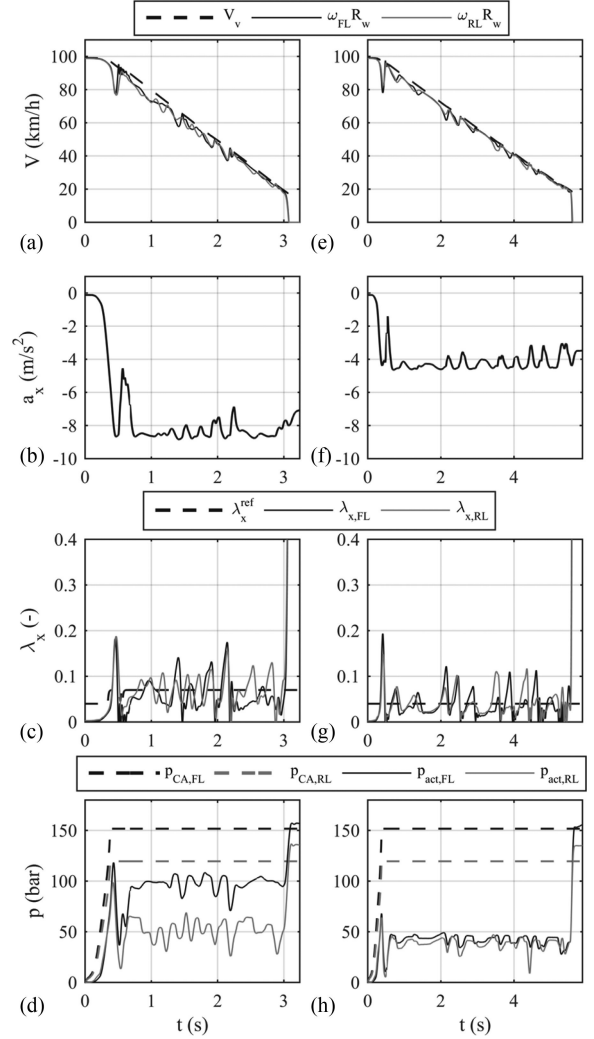

Fig. 9. Braking maneuver results: (a), (e) vehicle speed (V_v) and linear wheel speed ($\omega_i R_w$); (b), (f) longitudinal acceleration; (c), (g) tire slip ratio; (d), (h) regulated (p_{act}) and nonregulated (p_{CA}) caliper pressures. The left column refers to high-friction conditions; the right column refers to low-friction conditions.

Two road friction scenarios are considered, with friction coefficients, μ, of 0.9 and 0.45.

Fig. 9(a)–(d) reports the eNMPC ABS test results for the high-friction scenario, while Fig. 9(e)–(h) refers to the low-friction conditions. The online adaptive identification of the optimal reference slip ratio is not a part of this research, which focuses on the preliminary demonstration of eNMPC as a feedback control structure for ABS control. Therefore, in Fig. 9 the eNMPC ABS operated without retuning with two reference values of the slip ratio, i.e., 0.07 for the relevant part of the test at $\mu = 0.9$, and 0.04 for the test at $\mu = 0.45$. The transition between these values was based on longitudinal vehicle acceleration thresholds, providing a sufficiently good approximation of the available tire-road friction level. The reference slip ratio values, λ_x^{ref}, were computed from the longitudinal tire force characteristics as functions of slip ratio, by using the Pacejka MF, as reported in Fig. 10. For each front and rear tire, the vertical load at which the longitudinal force characteristic is calculated in Fig. 10 is
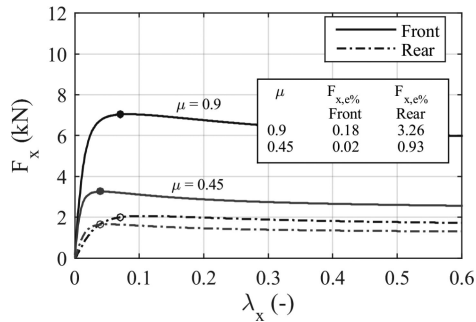
Fig. 10. Longitudinal tire force characteristics for different braking conditions.

the one corresponding to the maximum obtainable vehicle deceleration level on the specific road surface. For both the considered tire-road friction levels, the selected reference slip ratio is reasonably close to the longitudinal force peak. In fact, the percentage difference, $F_{x,e\%}$, between the longitudinal force at the adopted λ_x^{ref} and the maximum available longitudinal force is negligible (see the table included in Fig. 10). This confirms the insignificant advantage that a slightly higher reference slip ratio would have in terms of stopping distance, at the expense of reduced vehicle steerability.

Fig. 9(a) and (e) shows that the eNMPC avoids wheel locking until the ABS is deactivated at speeds less than 20 km/h. In Fig. 9(c) and (g), after the first peak, λ_x is appropriately controlled and oscillates around λ_x^{ref}. The satisfactory performance for both the μ conditions highlights the controller robustness against the variations in tire-road friction level. The longitudinal vehicle acceleration [see Fig. 9(b) and (f)] smoothly settles to approximately –8.5 and –4.5 m/s^2 during the high- and low-friction tests.

The pressure regulation profiles are shown in Fig. 9(d) and (h). As expected, the average values of the front and rear pressure output by the ABS change with the two friction conditions. In particular, the front-to-rear pressure ratio reduces from ∼2 at $\mu = 0.9$ to ∼1 at $\mu = 0.45$, because of the reduced vehicle deceleration resulting in lower vertical axle load transfer. Such variation of the average operating pressure has an important consequence on the controller design. In fact, as the EHB system dead time varies with p_{dem} (see Fig. 4), which, in turn, is influenced by the tire-road friction level, the dead time compensation strategy needs to be adaptable. In particular, the compensation should be based on different dead times for the two axles, or even for the individual wheels. In the proposed implementation, the dead time values on the front and rear axles are scheduled with the longitudinal vehicle deceleration. To assess this strategy, eNMPC ABS tests without dead time compensation and tests with incorrect dead time compensation values were performed. The results showed significant decay of the eNMPC's performance characteristics, especially in terms of greater slip ratio oscillation amplitudes. This is an important conclusion of this paper, made possible by the experimental characterization of the plant in Section II-C.

In addition, as the internal model considers only constant vertical tire loads (see Section IV-B), the good HiL results

further highlight the robustness of the eNMPC ABS approach and confirm the findings in [25]. The introduction of time-varying vertical tire loads as further eNMPC parameters would be possible, e.g., based on quasi-static assumptions. However, this would increase the offline computation time and, more importantly, the online memory utilization, which may increase the cost of the electronic control unit in series production.

To objectively compare the HiL results, the following performance indicators were used:

1) The stopping distance, d_{ABS}, i.e., the distance covered by the ABS-controlled vehicle to come to a stop after the brakes were applied.
2) The percentage difference, ERR, between d_{ABS} and the corresponding stopping distance of the passive vehicle, d_{passive}, i.e., the baseline stopping distance with locked wheels, measured during HiL braking tests for the vehicle without ABS. ERR is given as follows:

$$ERR = \frac{d_{\mathrm{ABS}} - d_{\mathrm{passive}}}{d_{\mathrm{passive}}} \cdot 100. \qquad (24)$$

3) The maximum value of the slip ratio, $\lambda_{x,\mathrm{peak}}$, during the ABS intervention.
4) The root-mean square value of the slip ratio error, $RMSE$, given as follows, in the relevant part of the test defined by the time interval $[t_i, t_e]$:

$$RMSE = \sqrt{\frac{1}{t_e - t_i} \int_{t_i}^{t_e} \left(\lambda_x\left(t\right) - \lambda_x^{\mathrm{ref}}\right)^2 dt}. \qquad (25)$$

5) The normalized integral of the absolute value of the torque reduction control action, $IACA$, given as follows, which quantifies the control effort during the interval $[t_i, t_e]$:

$$IACA = \frac{1}{t_e - t_i} \int_{t_i}^{t_e} \left|\Delta T\left(t\right)\right| dt. \qquad (26)$$

Table IV reports the performance indicator values for the straight-line braking tests from speed values of 100, 80, and 60 km/h, each of them for $\mu = 0.9$ and $\mu = 0.45$. Also, a braking test from a speed of 100 km/h was performed, with a sudden μ variation from 0.9 to 0.45. For the passive vehicle, the stopping distances are 66.20, 45.28, and 28.64 m for $\mu = 0.9$; the stopping distances are 118.97, 77.80, and 45.69 m for $\mu = 0.45$; the stopping distance is 89.77 m in the varying-μ scenario.

In addition to the eNMPC ABS results, the table includes the performance indicators for a benchmarking ABS controller. This consists of a PID controller of the slip ratio error, with anti-windup features. The PID gains were tuned along high tire-road friction straight-line braking tests simulated with the IPG CarMaker model. The optimal PID gains were selected using the Pattern Search function of MATLAB, so that the $RMSE$ of the slip ratio (i.e., the cost function of the optimization) was minimized, while the gain margin (GM) and phase margin (PM) of the open-loop transfer function had to exceed the set limits (i.e., $GM \geq 2$, $PM \geq 30°$, according to [48]), which were evaluated using a linearized model of the slip dynamics, as presented in [6]. The optimized gains were then implemented

TABLE IV
PERFORMANCE INDICATORS FOR THE PERFORMED HiL TESTS

	μ	$V_{v,\text{init}}$ (km/h)	d_{ABS} (m)	ERR (%)	$\lambda_{x,\text{peak}}$ (-)				$RMSE$ (-)				$IACA$ (Nm)			
					FL	FR	RL	RR	FL	FR	RL	RR	FL	FR	RL	RR
eNMPC	0.9	100	60.05	-9.29	0.18	0.18	0.19	0.19	0.04	0.04	0.03	0.04	1305	1367	1087	1108
		80	42.12	-6.99	0.15	0.15	0.17	0.18	0.03	0.04	0.05	0.04	1388	1323	1121	1101
		60	27.28	-4.74	0.16	0.16	0.19	0.24	0.04	0.04	0.05	0.06	1301	1277	1077	1115
	0.45	100	100.21	-15.77	0.19	0.19	0.14	0.14	0.03	0.03	0.03	0.03	2648	2653	1095	1094
		80	66.45	-14.58	0.21	0.21	0.16	0.16	0.03	0.03	0.03	0.03	2612	2647	1083	1090
		60	40.41	-11.57	0.23	0.22	0.18	0.18	0.04	0.04	0.03	0.03	2642	2682	1058	1088
	0.9/0.45	100	78.77	-12.55	0.39	0.57	0.17	0.17	0.06	0.08	0.04	0.04	2379	2356	1079	1104
PID	0.9	100	62.74	-5.24	0.56	0.66	0.63	0.64	0.10	0.12	0.13	0.16	1580	1549	975	985
		80	43.67	-3.56	0.69	0.76	0.71	0.72	0.13	0.16	0.17	0.19	1668	1663	941	1007
		60	28.28	-1.26	0.81	0.93	0.87	0.85	0.17	0.21	0.23	0.23	1600	1719	946	940
	0.45	100	107.03	-10.3	0.99	0.99	0.84	0.80	0.16	0.17	0.15	0.14	2843	2839	1118	1104
		80	73.52	-5.50	1.00	1.00	0.87	0.88	0.19	0.22	0.18	0.20	2944	2909	1095	1096
		60	45.62	-0.16	1.00	1.00	1.00	1.00	0.55	0.55	0.50	0.52	3212	3233	997	1014
	0.9/0.45	100	84.60	-5.75	1.00	1.00	1.00	1.00	0.22	0.27	0.21	0.23	2614	2657	1045	1021

on the HiL rig and further empirically fine-tuned on the basis of the reduction of the $RMSE$ value for consecutive tests in high tire-road friction conditions from 100 km/h. The same PID gains were used for the low friction HiL tests.

For $V_{v,\text{init}} = 100\,\text{km/h}$, the eNMPC ABS achieves stopping distance reductions of 9.29% and 15.77% on the high- and low-friction surfaces, with respect to the passive vehicle. For all vehicle corners, the slip ratio peak never exceeds 0.19 in the high- and low-friction scenarios, for this initial speed. The $IACA$ shows ~1000–1300 Nm torque reductions on the front and rear axles on the high-friction surface [see Fig. 9(d)], while in the low-friction scenario, the torque regulation is ~2500 Nm on the front axle and ~1000 Nm on the rear axle. Similar performance levels are obtained for the tests from 80 and 60 km/h, and the varying-μ test from the speed of 100 km/h, which demonstrates the suitability of the eNMPC ABS for a wide range of braking conditions.

The PID ABS always yields longer stopping distances than those achieved by the eNMPC ABS. The ERR difference between the two controllers is approximately 3%–4% in high-friction conditions (depending on $V_{v,\text{init}}$), and it becomes more substantial in low-friction conditions (up to 11.4%).

Moreover, with the PID ABS, $\lambda_{x,\text{peak}}$ reaches 0.66 and 0.99 on the high- and low-friction surfaces for the tests for speed values from 100 km/h, while the same controller generates temporary wheel locking during the tests for speed values from 80 and 60 km/h at $\mu = 0.45$. Such high values of the maximum slip ratio are registered immediately after the initial ABS activation, during the first ABS cycle, after which the PID ABS tracking performance measured using the $RMSE$ is rather good, despite being inferior to that of the eNMPC ABS. The lack of robustness of the PID ABS is consistent with the results in [9].

The promising results of the eNMPC ABS highlight the potential of such a control technology for future industrial assessment for wheel slip control applications.

VII. CONCLUSION

This paper discussed the proof-of-concept design of an eN-MPC for ABS, its implementation on an industrial EHB unit,

and the experimental comparison with a PID ABS. The analysis led to the following conclusions:

1) The experimental step response of the case-study EHB system showed significant variations of the pressure dead time and rise time as functions of the final pressure value. As the measured dead times of ~20 ms are much longer than the ABS controller time step of 3 ms, the proposed dead time compensation strategy is an important component of the eNMPC ABS.

2) The experimental braking test results showed the eN-MPC robustness with respect to the tire-road friction conditions and initial speed. A satisfactory performance was obtained with a relatively simple internal model formulation, which neither considered actuation dynamics nor vertical tire load variation. Conversely, the dead time compensation strategy was necessary to ensure the correct performance of the controller.

3) The online computation time for the explicit solution was assessed on an automotive rapid control prototyping unit to be $< 95\,\mu$s, which confirmed the real-time capability of the eNMPC ABS for any implementation time step typical of ABS applications. The memory requirements were also in-line with the available automotive microcontroller units (up to 16 MB).

4) The eNMPC ABS consistently outperformed the PID ABS; e.g., it reduced the stopping distance in low tire-road friction conditions by up to 11.4%. These results make eNMPC a promising technology for automotive wheel slip control applications.

REFERENCES

[1] Z. Tianjun and Z. Changfu, "Research on electro-hydraulic brake system for vehicle stability," in *Proc. Int. Conf. Ind. Inf. Syst.*, 2009, pp. 344–347.

[2] E. Nakamura, M. Soga, A. Sakai, and T. Kobayashi, "Development of electronically controlled brake system for hybrid vehicle," SAE Tech. Paper 2002-01-0300, 2002.

[3] V. Ivanov, D. Savitski, and B. Shyrokau, "A survey of traction control and anti-lock braking systems of full electric vehicles with individually controlled electric motors," *IEEE Trans. Veh. Technol.*, vol. 64, no. 9, pp. 3878–3896, Sep. 2015.

[4] D. Savitski, V. Ivanov, D. Schleinin, K. Augsburg, T. Pütz, and C. F. Lee, "Advanced control functions of decoupled electro-hydraulic brake system," in *Proc. IEEE 14th Int. Workshop Adv. Motion Control*, 2016, pp. 310–317.

[5] N. D'Alfio, A. Morgando, and A. Sorniotti, "Electro-hydraulic brake system: Design and test through hardware-the-loop simulation," *Veh. Syst. Dyn.*, vol. 44, no. 1, pp. 378–392, 2006.

[6] M. S. Savaresi and M. Tanelli, *Active Braking Control System Design for Vehicles*, New York, NY, USA: Springer-Verlag, 2010.

[7] A. A. Aly, E.-S. Zeidan, A. Hamed, and F. Salem, "An antilock-braking systems (ABS) control: A technical review," *Intell. Control Autom.*, vol. 2, no. 3, pp. 186–195, 2011.

[8] S. B. Choi, "Antilock brake system with a continuous wheel slip control to maximize the braking performance and the ride quality," *IEEE Trans. Control Syst. Technol.*, vol. 16, no. 5, pp. 996–1003, Sep. 2008.

[9] D. Savitski, D. Schleinin, V. Ivanov, and K. Augsburg, "Robust continuous wheel slip control with reference adaptation: Application to brake system with decoupled architecture," *IEEE Trans. Ind. Inf.*, vol. 14, no. 9, pp. 4212–4223, Sep. 2018 (in press).

[10] S. de Pinto, C. Chatzikomis, A. Sorniotti, and G. Mantriota, "Comparison of traction controllers for electric vehicles with on-board drivetrains," *IEEE Trans. Veh. Technol.*, vol. 66, no. 8, pp. 6715–6727, Aug. 2017.

[11] V. R. Aparow, F. Ahmad, K. Hudha, and H. Jamaluddin, "Modelling and PID control of antilock braking system with wheel slip reduction to improve braking performance," *Int. J. Veh. Saf.*, vol. 6, no. 3, p. 265–296, 2013.

[12] M. Amodeo, A. Ferrara, R. Terzaghi, and C. Vecchio, "Wheel slip control via second-order sliding-mode generation," *IEEE Trans. Intell. Transp. Syst.*, vol. 11, no. 1, pp. 122–131, Mar. 2010.

[13] D. Yin, S. Oh, and Y. Hori, "A novel traction control for EV based on maximum transmissible torque estimation," *IEEE Trans. Ind. Electron.*, vol. 56, no. 6, pp. 2086–2094, Jun. 2009.

[14] H. Fujimoto, J. Amada, and K. Maeda, "Review of traction and braking control for electric vehicle," in *Proc. IEEE Veh. Power Propulsion Conf.*, 2012, pp. 1292–1299.

[15] Y. Wang, H. Fujimoto, and S. Hara, "Driving force distribution and control for EV with four in-wheel motors: A case study of acceleration on split-friction surfaces," *IEEE Trans. Ind. Electron.*, vol. 64, no. 4, pp. 3380–3388, Apr. 2017.

[16] T. A. Johansen, I. Petersen, J. Kalkkuhl, and J. Ludemann, "Gain-scheduled wheel slip control in automotive brake systems," *IEEE Trans. Control Syst. Technol.*, vol. 11, no. 6, pp. 799–811, Nov. 2003.

[17] C. Satzger, R. de Castro, A. Knoblach, and J. Brembeck, "Design and validation of an MPC-based torque blending and wheel slip control strategy," in *Proc. IEEE Intell. Veh. Symp. (IV)*, 2016, vol. 2016–August, no. iv, pp. 514–520.

[18] C. Satzger and R. de Castro, "Combined wheel slip control and torque blending using MPC," in *Proc. Int. Conf. Connect. Veh. Expo*, 2014, pp. 618–624.

[19] R. de Castro, R. E. Araújo, M. Tanelli, and S. M. Savaresi, "Torque blending and wheel slip control in EVs with in-wheel motors," *Veh. Syst. Dyn.*, vol. 50, no. sup1, pp. 71–94, 2012.

[20] C. Satzger and R. de Castro, "Predictive brake control for electric vehicles," *IEEE Trans. Veh. Technol*, vol. 67, no. 2, pp. 977–990, Feb. 2018.

[21] D. Yoo and L. Wang, "Model based wheel slip control via constrained optimal algorithm," in *Proc. IEEE Int. Conf. Control Appl.*, 2007, pp. 1239–1246.

[22] F. Borrelli, A. Bemporad, M. Fodor, and D. Hrovat, "An MPC/hybrid system approach to traction control," *IEEE Trans. Control Syst. Technol.*, vol. 14, no. 3, pp. 541–552, May. 2006.

[23] M. S. Basrah, E. Siampis, E. Velenis, D. Cao, and S. Longo, "Wheel slip control with torque blending using linear and nonlinear model predictive control," *Veh. Syst. Dyn.*, vol. 55, no. 11, pp. 1665–1685, 2017.

[24] L. Yuan, H. Zhao, H. Chen, and B. Ren, "Nonlinear MPC-based slip control for electric vehicles with vehicle safety constraints," *Mechatronics*, vol. 38, pp. 1–15, 2016.

[25] D. Tavernini, M. Metzler, P. Gruber, and A. Sorniotti, "Explicit nonlinear model predictive control for electric vehicle traction control," *IEEE Trans. Contr. Syst. Technol.*, to be published, doi: 10.1109/TCST.2018.2837097.

[26] A. Bemporad, D. Bernardini, R. Long, and J. Verdejo, "Model predictive control of turbocharged gasoline engines for mass production," SAE Tech. Paper 2018-01-0875, 2018.

[27] E. Siampis, E. Velenis, S. Gariuolo, and S. Longo, "A real-time nonlinear model predictive control strategy for stabilization of an electric vehicle at the limits of handling," *IEEE Trans. Control Syst. Technol.*, vol. 26, no. 6, pp. 1982–1994, Nov. 2018.

[28] B. J. Ganzel, "Slip control boost braking system," U.S. Patent 9 221 443 B2, 2015.

[29] L. de Novellis *et al.*, "Direct yaw moment control actuated through electric drivetrains and friction brakes: Theoretical design and experimental assessment," *Mechatronics*, vol. 26, pp. 1–15, 2015.

[30] D. Savitski, "Robust control of brake systems with decoupled architecture," Ph.D. dissertation, Autom. Eng. Group, Technische Universität Ilmenau, Illmenau, Germany, 2019.

[31] H. B. Pacejka, *Tire and Vehicle Dynamics*. Amsterdam, The Netherlands: Elsevier, 2012.

[32] E. Giangiulio and D. Arosio, "New validated tire model to be used for ABS and VDC simulations," in *Proc. 3rd Int. Colloquium Veh.-Tyre-Road Interact.*, 2006, pp. 1–17.

[33] J. A. Grancharova and T. A. Johansen, *Explicit Nonlinear Model Predictive Control: Theory and Applications*, vol. 429. New York, NY, USA: Springer-Verlag, 2012.

[34] T. A. Johansen, "On multi-parametric nonlinear programming and explicit nonlinear model predictive control," in *Proc. 41st IEEE Conf. Decis. Control.*, 2002, vol. 3, pp. 2768–2773.

[35] L. F. Domínguez and E. N. Pistikopoulos, "Recent advances in explicit multiparametric nonlinear model predictive control," *Ind. Eng. Chem. Res.*, vol. 50, no. 2, pp. 609–619, 2011.

[36] P. Tøndel and T. A. Johansen, "Lateral vehicle stabilization using constrained nonlinear control," in *Proc. Eur. Control Conf.*, 2003, pp. 1887–1892.

[37] M. Herceg, M. Kvasnica, C. N. Jones, and M. Morari, "Multi-parametric toolbox 3.0," in *Proc. Eur. Control Conf.*, 2013, pp. 502–510.

[38] A. Wächter and L. T. Biegler, "On the implementation of a primal-dual interior point filter line search algorithm for large-scale nonlinear programming," *Math. Program.*, vol. 106, no. 1, pp. 25–57, 2006.

[39] P. Tøndel, T. A. Johansen, and A. Bemporad, "Evaluation of piecewise affine control via binary search tree," *Automatica*, vol. 39, no. 5, pp. 945–950, 2003.

[40] R. Limpert, *Brake Design and Safety*. Warrendale, PA, USA: SAE, 1999.

[41] M. Jalaliyazdi, A. Khajepour, S. Chen, and B. Litkouhi, "Handling delays in stability control of electric vehicles using MPC," SAE Tech. Paper 2015-01-1598, Apr. 2015.

[42] H. Chen and F. Allgöwer, "A quasi-infinite horizon nonlinear model predictive control scheme with guaranteed stability," *Automatica*, vol. 34, no. 10, pp. 1205–1217, 1998.

[43] D. Q. Mayne, J. B. Rawlings, C. V. Rao, and P. O. M. Scokaert, "Constrained model predictive control: Stability and optimality," *Automatica*, vol. 36, no. 6, pp. 789–814, 2000.

[44] L. Grüne, "Analysis and design of unconstrained nonlinear MPC schemes for finite and infinite dimensional systems," *SIAM J. Control Optim.*, vol. 48, no. 2, pp. 1206–1228, 2009.

[45] M. Reble and F. Allgöwer, "Unconstrained model predictive control and suboptimality estimates for nonlinear continuous-time systems," *Automatica*, vol. 48, no. 8, pp. 1812–1817, 2012.

[46] "Regulation No 13 of the Economic Commission for Europe of the United Nations (UN/ECE)—Uniform provisions concerning the approval of vehicles of categories M, N and O with regard to braking," Official Journal of the European Union, 2010.

[47] International Standard "Passenger cars - Stopping distance at straight-line braking with ABS - Open-loop test method" Reference number: ISO 21994:2007.

[48] S. Skogestad and I. Postlethwaite, *Multivariable Feedback Control: Analysis and Design*. Hoboken, NJ, USA: Wiley, 2007.

Davide Tavernini received the M.Sc. degree in mechanical engineering and the Ph.D. degree in dynamics and design of mechanical systems, from the University of Padova, Padua, Italy, in 2010 and 2014, respectively.

He is a Lecturer in Advanced Vehicle Engineering with the University of Surrey, Guildford, U.K. His research interests include vehicle dynamics modeling and control, mostly applied to electric and hybrid electric vehicles.

Fabio Vacca received the M.Sc. degree in mechanical engineering from the Politecnico di Bari, Bari, Italy, in 2013. He is currently working toward the Ph.D. degree in automotive engineering with the University of Surrey, Guildford, U.K.

His research interests include hybrid electric vehicles, electric vehicles, and vehicle dynamics.

Patrick Gruber received the M.Sc. degree in motorsport engineering and management from Cranfield University, Cranfield, U.K., in 2005, and the Ph.D. degree in mechanical engineering from the University of Surrey, Guildford, U.K., in 2009.

He is a Reader in Advanced Vehicle Systems Engineering with the University of Surrey. His research interests include vehicle dynamics and tire dynamics with special focus on friction behavior.

Mathias Metzler (GSM'17) received the Dipl.-Ing. degree in mechanical engineering from the Vienna University of Technology, Vienna, Austria, in 2015. He is currently working toward the Ph.D. degree in advanced vehicle engineering with the University of Surrey, Guildford, U.K.

His research interests include vehicle dynamics control, model predictive control, optimization and nonlinear systems.

Ahu Ece Hartavi received the M.Sc. and Ph.D. degrees in electrical engineering from Istanbul Technical University, Istanbul, Turkey, in 2000 and 2006, respectively.

She is a Senior Lecturer in Intelligent Vehicles with the University of Surrey, Guildford, U.K. Her research interests include intelligent control, electric vehicle modeling and control, and automated vehicles.

Dzmitry Savitski (S'12–M'18) received the Dipl.-Ing. degree in automotive engineering from Belarusian National Technical University, Minsk, Belarus, in 2011, and the Dr.-Ing. degree in automotive engineering with the Technische Universität Ilmenau (TUIL), Ilmenau, Germany, in 2019.

He is now a Lead Engineer with Arrival Germany GmbH, Pforzheim, Germany, and develops control software for X-by-Wire chassis systems.

Miguel Dhaens received the M.Sc. degree in electro-mechanical engineering from Katholiek Industriële Hogeschool (KIH), Ostend, Belgium, in 1993.

He is an Engineering Manager with the Global Research Ride Performance Team, Tenneco, Lake Forest, IL, USA, and he is responsible for defining the research road map and coordinating the global research activities of Tenneco's Ride Performance business, which includes vehicle dynamics, damping solutions, mechatronics, material science, manufacturing technologies, and predictive tools. Before joining Tenneco, he was with the Formula One team of Toyota Motorsport GmbH, Germany, as a Manager of the engine, testing, and advanced strategies teams, and with Flanders Drive as an R&D Manager.

Valentin Ivanov (M'13–SM'15) received the Mech. Eng., Ph.D., and D.Sc. degrees in automotive engineering from Belarusian National Technical University, Minsk, Belarus, in 1992, 1997, and 2006, respectively, and the Dr.-Ing. Habil. grade in automotive engineering from the Technische Universität Ilmenau (TUIL), Ilmenau, Germany, in 2017.

From 1998 to 2007, he was an Assistant Professor, Associate Professor, and Full Professor with the Department of Automotive Engineering, Belarusian National Technical University. He is an European Project Coordinator with the Automotive Engineering Group at TUIL. His research interests include vehicle dynamics, electric vehicles, automotive control systems, and chassis design.

Aldo Sorniotti (M'12) received the M.Sc. degree in mechanical engineering and the Ph.D. degree in applied mechanics from the Politecnico di Torino, Turin, Italy, in 2001 and 2005, respectively.

He is a Professor in Advanced Vehicle Engineering with the University of Surrey, Guildford, U.K., where he coordinates the Centre for Automotive Engineering. His research interests include vehicle dynamics control and transmission systems for electric and hybrid electric vehicles.